JACS
JOURNAL OF THE AMERICAN CHEMICAL SOCIETY

Article

pubs.acs.org/JACS

Tempo-Spatially Resolved Scattering Correlation Spectroscopy under Dark-Field Illumination and Its Application to Investigate Dynamic Behaviors of Gold Nanoparticles in Live Cells

Heng Liu, Chaoqing Dong, and Jicun Ren*

College of Chemistry & Chemical Engineering, State Key Laboratory of Metal Matrix Composites, Shanghai Jiaotong University, Shanghai 200240, People's Republic of China

Supporting Information

ABSTRACT: In this study, a new tempo-spatially resolved fluctuation spectroscopy under dark-field illumination is described, named dark-field illumination-based scattering correlation spectroscopy (DFSCS). DFSCS is a single-particle method, whose principle is similar to that of fluorescence correlation spectroscopy (FCS). DFSCS correlates the fluctuations of the scattered light from single nanoparticle under dark-field illumination. We developed a theoretical model for translational diffusion of nanoparticles in DFSCS system. The results of computer simulations documented that this model was able to well describe the diffusion behaviors of nanoparticles in uniformly illuminated field. The experimental setup of DFSCS was achieved by introducing a dark-field condenser to the frequently used bright-field microscope and an electron multiplying charge-coupled device (EMCCD) as the array detector. In the optimal condition, a stack of 500 000 frames were collected simultaneously on 64 detection channels for a single measurement with acquisition rate of 0.5 ms per frame. We systematically investigated the effect of certain factors such as particle concentration, viscosity of the solution, and heterogeneity of gold nanoparticles (GNPs) samples on DFSCS measurements. The experiment data confirmed theoretical model proposed. Furthermore, this new method was successfully used for investigating dynamic behaviors of GNPs in live cells. Our preliminary results demonstrate that DFSCS is a practical and affordable tool for ordinary laboratories to investigate the dynamic information of nanoparticles *in vitro* as well as *in vivo*.

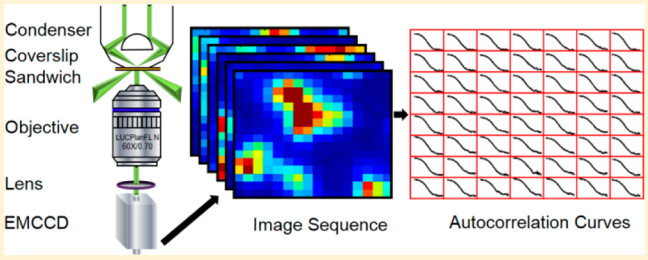

INTRODUCTION

As the basic unit of life, the cell is considered to be a complex, heterogeneous, and dynamic biosystem.[1] Therefore, only tempo-spatially resolved methods can reveal the spatial distribution of dynamic information about live cells, such as concentrations, mobilities, equilibrium, rate constants, and the interactions of biomolecules. As one progenitor of the field of single-molecule detections, fluorescence correlation spectroscopy (FCS) is a powerful and minimally invasive technique to measure these interesting parameters.[2] FCS can extract dynamic information at single-molecule level from fluctuations observed in the emission of fluorescent molecules in thermodynamic equilibrium. Since first being introduced 40 years ago,[3] FCS has been widely used to investigate the diffusion of molecules,[4] binding and reaction kinetics,[5] single-molecule photophysics,[6] and conformational dynamics of proteins[7] with its excellent temporal resolution and high statistical confidence.[8] At present, FCS is regarded as a routine tool to investigate the dynamic processes of single molecules in physics, chemistry, and biology.[9]

A key point to achieve FCS is the high signal-to-noise ratio (S/N) of measurements.[2,8a] Until the introduction of the confocal illumination scheme by Rigler et al. FCS underwent a renaissance.[8a] The confocal illumination defines a very small detection volume (usually ~1 fL) such that only very few molecules are present in the detection volume at any one time. With that, the background noise is low enough to yield high S/N. This configuration generated great technical improvements and pushed the sensitivity of FCS to single-molecule level. Unfortunately, the confocal apparatus is complex and vulnerable that even a slight optical aberration or saturation has significant impacts on the measurements.[10] Additionally, the commercial FCS systems[11] are still very expensive and usually cost more than 300 000 dollars. More importantly, the detection volume in the confocal FCS setup is considered as a "point". So it is difficult to perform FCS measurements on a large number of spots simultaneously, which is especially crucial when the objective system is heterogeneous, e.g., live cells. In recent years, certain methods derived from or related to FCS have been constantly springing up.[12] New illumination schemes and methodologies have been introduced, such as total internal reflection,[13] raster image correlation spectroscopy,[14] stimulated emission depletion,[15] single plane illumination,[16] and so on. Similarly, these nonconfocal schemes also define a very small or thin detection volume. However, to our knowledge, the dark-

Received: October 7, 2013
Published: January 26, 2014

   dx.doi.org/10.1021/ja410284j | J. Am. Chem. Soc. 2014, 136, 2775−2785

field configuration has not found a place in the family tree of FCS and related fluctuation correlation spectroscopy.

Since first developed to observe single metal particles by Zsigmondy and co-workers a century ago,[17] the dark-field microscopy has been a popular technique utilized to render unstained and transparent specimens clearly visible. It works on the principle of illuminating the sample with the light that will not be collected by the objective lens and thus will not form part of the image. This scheme produces the classic appearance of a dark (almost black) background with bright objects on it[18] and in turn yields high S/N. It inspires us that although the dark-filed microscopy is a nonconfocal illumination scheme, it may be employed to conduct fluctuation correlation spectroscopy measurements. Moreover, it is very easy to establish the dark-field configuration by installing a dark-field condenser (costs about 100 dollars) on a bright-field microscope. Nowadays the dark-field illumination is a standard mounting of the optical microscope.

One of the reasons for the absence of dark-field illumination in the FCS family is that previous investigations in the field of FCS mainly focus on the fluorescent molecules or fluorescent particles. To date, the major probes employed in FCS measurements are organic dyes as well as fluorescent proteins. These fluorophors provide high sensitivity and great versatility while minimally perturbing the live cells under investigation.[19] However, their inherent fluorescence decay or even bleaching severely limits the available observation time.[20] Another kind of fluorescent probes emerged in recent years is the semiconductor quantum dots (QDs). Although with the high quantum yield and greatly improved photostability,[21] most of the commonly used QDs are composed of heavy metals that are cytotoxic, such as the element cadmium, resulting in restrictions on certain biological and biomedical applications.[22] Fortunately, certain noble metal nanoparticles, especially gold nanoparticles (GNPs), have shown great promise to be the attractive alternative, due to ease of synthesis and functionalization, low toxicity, excellent chemical and photostability, and good biocompatibility.[23] GNPs also have been applied as fluorescent probes,[24] but their most exciting property is the strong, nonbleaching resonance light scattering (RLS)[25] with the efficiency equivalent to the fluorescent intensity of about 10^6 fluorophors.[26] RLS is a collective oscillation of the conduction electrons,[27] which results in extremely intensive absorption and large scattering cross sections of GNPs many times more than their geometric size.[28] On the basis of RLS of GNPs or silver nanoparticles, our laboratory has proposed two variants of FCS, which are termed resonance light scattering correlation spectroscopy (RLSCS)[29] and spatially resolved scattering correlation spectroscopy using a total internal reflection configuration (SRSCS),[30] respectively. The experimental results have demonstrated that GNPs are sensitive and stable as the probe for FCS. On the other hand, GNPs are also ideal probes for the dark-field microscopy on account of the markedly enhanced S/N by their strong RLS.[31]

In this paper, in order to combine the advantages of the dark-field microscopy and the unique optical properties of GNPs, a new tempo-spatially resolved fluctuation spectroscopy method using dark-field illumination mode and GNPs as the probes is described, which is named dark-field illumination-based scattering correlation spectroscopy (DFSCS). The principle of DFSCS is similar to that of FCS and RLSCS, and it measures the fluctuations of the scattered light in a small volume due to Brownian motion of nanoparticles. It should be pointed out that DFSCS differs from dynamic light scattering (DLS) because DFSCS, similar to FCS, is cast in terms of space-time concentration fluctuation correlation. Additionally, the size and profile of the detection volume have to be taken into account for DFSCS measurements.[3b] Besides, DLS is not a single-particle method.[32] The differences were further illustrated by their distinct theoretical models mentioned in this paper. We set up the DFSCS system based on a bright-field microscope with a dark-field condenser, and a highly sensitive and fast-response EMCCD camera was used as an array detector. The theoretical model of DFSCS was deduced, and its reliability and adaptability were tested by simulated results and experimental data. After calibrations, we utilized DFSCS to systematically investigate the concentration and diffusion coefficient of nanoparticles and the heterogeneity of samples. In addition, the sensitivity of the new method was studied in theory as well as in experiments. Based on the above fundamental works, we applied DFSCS to investigate the dynamic information of single GNPs in live cells and characterize the heterogeneous intracellular environment.

THEORY

The dark-field illumination is different from the existing configurations in FCS. Therefore, the theoretical model of DFSCS should be first established. In this part, we compute the temporal autocorrelation function, $G(t)$, of the fluctuations of the scattered intensity from nanoparticles illuminated in the dark-field microscope. Samples of nanoparticles are maintained at thermodynamic equilibrium. However, they are continually fluctuating around the equilibrium. These fluctuations are due to random variations in the number of nanoparticles in a defined volume as a result of diffusion, chemical reaction, and so on. Since the kinetic coefficients corresponding to these processes determine the dynamics of their relaxation, which in turn determines the profile of $G(t)$, a complete kinetic description of these processes can be achieved through the analysis of $G(t)$ according to an appropriate theoretical model. The model expresses $G(t)$ in terms of phenomenological coefficients for diffusion and chemical reaction. Here, we present the derivation of the theoretical model of DFSCS on the basis of FCS theory proposed by Elson and Magde in 1974[3b] as well as by Krichevsky and Bonnet in 2002[32] with some modifications introduced.

General Formalism. Here we consider an ideal solution containing m kinds of nanoparticles. Let the concentration (number of nanoparticles per unit of volume) of the nanoparticles j at position $\vec{r}$ and time t be $C_j(\vec{r},t)$, its ensemble average concentration be $\overline{c}_j = \langle C_j(\vec{r},t)\rangle$ ($\langle\ \rangle$ denotes ensemble average) and the local deviation be $\delta C_j(\vec{r},t) = C_j(\vec{r},t) - \overline{c}_j$. $\delta C_j(\vec{r},t)$ is determined by diffusion and chemical reaction and so on. The intensity profile of the illumination light at position $\vec{r}$ is denoted by $I(\vec{r})$. The deviations of $Cj(\vec{r},t)$ in a defined volume cause fluctuations of the scattered light and in turn determine the fluctuations of the photons collected by the detector. It is assumed that the number of photons scattered and detected from each nanoparticle is proportional to $I(\vec{r})$, hence the number of detected photons $n(t)$ per sample time Δt is

$$n(t) = \Delta t \int d^3\vec{r} I(\vec{r}) \sum_{k=1}^{m} Q_k C_k(\vec{r}, t) \quad (1)$$

dx.doi.org/10.1021/ja410284j | J. Am. Chem. Soc. 2014, 136, 2775−2785

where Q_k is combined from the absorption cross section and scattering efficiency of nanoparticles k. Then the deviation of the photon count $\delta n(t)$ from the ensemble average $\overline{n} = \langle n(t)\rangle$ is

$$\delta n(t) = n(t) - \overline{n} = \Delta t \int d^3\vec{r} I(\vec{r}) \sum_{k=1}^{m} Q_k \delta C_k(\vec{r}, t) \tag{2}$$

In FCS theory, the normalized $G(t)$, which measures the correlation between the intensity F detected at a certain time t' and that detected at time t later, is expressed as[33]

$$g(t) = \langle F(t')F(t' + t)\rangle/\langle F\rangle^2 = 1 + \langle \delta F(t')\delta F(t' + t)\rangle/\langle F\rangle^2 = 1 + G(t) \tag{3}$$

here δF is the fluctuation of fluorescent intensity, $\delta F = F(t') - \langle F(t')\rangle$. For simplicity $|t|$ is written as t in the following. Similarly, $G(t)$ in DFSCS is defined as the time average of the products of the intensity fluctuations and normalized by the square of the ensemble average $\overline{n}^2$

$$G(t) = \frac{1}{\overline{n}^2 T} \sum_{i=0}^{T-1} \delta n(t')\delta n(t' + t) \tag{4}$$

where T is the total sampling number, t is the delay time corresponding to the delay channel m such that $m = t/\Delta t$; $\delta n(t') = n_i - \overline{n}$, $\delta n(t' + t) = n_{i+m} - \overline{n}$, where n_i, n_{m+i} are the numbers of photon counts collected at times $t' = i\Delta t$ and $t' + t = (i + m)\Delta t$, respectively.

Therefore, the experimental manifestation of the correlation of concentration fluctuations is the temporal autocorrelation of the collected photons (the process of derivation is outlined in the Supporting Information)

$$G(t) = \frac{(2\pi)^{-3}(\Delta t)^2}{\overline{n}^2} \int d^3\vec{q}\, |\tilde{I}(\vec{q})|^2 \sum_{j,l} Q_j Q_l \overline{C}_j \sum_{s=1}^{m} X_l^{(s)} \exp(\lambda^{(s)} t)(X^{-1})_j^{(s)} \tag{5}$$

where $\tilde{I}(\vec{q}) = \int d^3\vec{r} e^{-I\vec{q}\vec{r}} I(\vec{r})$ is the Fourier transform of $I(\vec{r})$, $\overline{n}$ is the average number of the detected photons $\overline{n} = \Delta t \int d^3\vec{r} I(\vec{r}) \sum_{i=1}^{m} Q_i \overline{C}_i = \tilde{I}(0)\Delta t \sum_{i=1}^{m} Q_i \overline{C}_i$, $\overline{C}_j$ denotes the mean-square fluctuations of $C_j(\vec{r}',t)$ of nanoparticles in a defined volume, which is equal to its average $\langle C_j(\vec{r}',t)\rangle$ for Poisson statistics, $X_l^{(s)}$ are the components of the right eigenvectors corresponding to the eigenvalue $\lambda^{(s)}$ of the matrix M ($M_{jk} = K_{jk} - D_l q^2 \delta_{jk}$, D_j denotes the diffusion coefficient of nanoparticle j, and coefficients K_{jk} are composed of chemical rate constants and the equilibrium concentrations of the species), and X^{-1} is the inverse matrix of eigenvectors.

Now $G(t)$ is expressed as a function of the concentration, diffusion coefficient and chemical rate. The remaining determinants of $G(t)$ are parameters of the experimental setup, among which the most important one is the intensity profile of the illumination light $I(\vec{r})$. In confocal FCS, the intensity distribution is usually treated as Gaussian[32] or Gaussian−Lorentzian.[34] The dark-field microscopy is a wide-field illumination method, and the diameter of its excitation area is centimeter scale, which is much larger than an individual detection volume (<1 μm). Additionally, the light in the illumination area is a quasi-parallel beam. Based on the foregoing two reasons, we treat the intensity distribution in the detection volume of DFSCS as a uniform field. As a variant of imaging FCS,[35] DFSCS employs a camera as the detector, and each pixel of the camera becomes an independent inspection window. Since the illumination intensity is homogeneous, the cross talk between the neighboring pixels is mutual, and their amplitudes are comparative, we assume that each pixel mainly collects the scattered light from its corresponding illuminated area that directly faces this pixel, where the cross talk from the neighboring illuminated area is ignored.[9b,36] Thus the optical path length between the pixel and its corresponding illuminated area for all detection volumes is identical. As a result, the collection efficiency function in the detection volume is homogeneous, too. In summary, each pixel is an integral and square-shape detector with identical collection efficiency. A three-dimension Cartesian coordinate system is established, and its origin is located at the center of the detection volume. The z-axis is chosen to be along the optical axis of the objective. Therefore, the intensity profile in a detection volume of $2a$ length, $2c$ width, and $2h$ height is described as

$$\begin{cases} I(\vec{r}) = I_0, |\vec{r}_x| \le a, |\vec{r}_y| \le c, |\vec{r}_z| \le h \\ I(\vec{r}) = 0, \text{elsewhere} \end{cases} \tag{6}$$

here, I_0 is the illumination intensity at the origin, and $\vec{r}_x$, $\vec{r}_y$, and $\vec{r}_z$ are the projections of $\vec{r}$ onto the x, y, and z axes, respectively.

Next, a Fourier transform is conducted to eq 6

$$\tilde{I}(\vec{q}) = \int d^3\vec{r} e^{-i\vec{q}\vec{r}} I(\vec{r}) = I_0 \frac{2}{q_x}\sin(aq_x)\frac{2}{q_y}\sin(cq_y)\frac{2}{q_z}\sin(hq_z) \tag{7}$$

The average number of the detected photons $\overline{n}$ is

$$\overline{n} = \tilde{I}(0)\Delta t \sum_{i=1}^{m} Q_i \overline{C}_i = \lim_{\vec{q}\to 0}[\tilde{I}(\vec{q})]\Delta t \sum_{i=1}^{m} Q_i \overline{C}_i = 8achI_0\Delta t \sum_{i=1}^{m} Q_i \overline{C}_i \tag{8}$$

Then, substituting eqs 7 and 8 into eq 5 yields

$$G(t) = \frac{(2\pi)^{-3}}{(ach\sum_{s=1}^{m} Q_i \overline{C}_i)^2} \int d^3\vec{q} \begin{bmatrix} \frac{1}{q_x^2}\sin^2(aq_x)\frac{1}{q_y^2}\sin^2(cq_y) \\ \frac{1}{q_z^2}\sin^2(hq_z) \end{bmatrix} \sum_{j,l} Q_j Q_l \overline{C}_j \sum_{s=1}^{m} X_l^{(s)} \exp(\lambda^{(s)} t)(X^{-1})_j^{(s)} \tag{9}$$

In this paper, we focus on the simplest case: diffusion of one kind of nanoparticle in a dilute solution

$$\frac{\partial \delta C(\vec{r}, t)}{\partial t} = D\nabla^2 \delta C(\vec{r}, t) \tag{10}$$

Then, a Fourier transform is applied to eq 10

$$\delta C(\vec{q}, t) = \delta C(\vec{q}, 0)\exp(-D\vec{q}^2 t) \tag{11}$$

The matrix M has only one set of solution: the eigenvalue $\lambda = -Dq^2$, with its corresponding eigenvector $X = 1$. Substituting these values into eq 9 we obtain

$$G(t) = \frac{1}{\pi^{3/2} ach\overline{N}} \left[\exp\left(-\frac{a^2}{Dt}\right)\sqrt{Dt} + a\sqrt{\pi}\,\mathrm{erf}\left(\frac{a}{\sqrt{Dt}}\right) - \sqrt{Dt}\right] \times \left[\exp\left(-\frac{c^2}{Dt}\right)\sqrt{Dt} + c\sqrt{\pi}\,\mathrm{erf}\left(\frac{c}{\sqrt{Dt}}\right) - \sqrt{Dt}\right] \times \left[\exp\left(-\frac{h^2}{Dt}\right)\sqrt{Dt} + h\sqrt{\pi}\,\mathrm{erf}\left(\frac{h}{\sqrt{Dt}}\right) - \sqrt{Dt}\right] \tag{12}$$

where $V = 8ach$ is the detection volume, $\overline{N} = V\overline{c} = 8ach\overline{c}$ is the average number of particles in the detection volume, and erf is the error function. The pixel of the frequently used camera is

dx.doi.org/10.1021/ja410284j | J. Am. Chem. Soc. 2014, 136, 2775−2785

square, thus $a = c$. Besides, we define the aspect ratio of the detection volume as $\omega = h/a$ and the characteristic diffusion time across the detection volume as $\tau_D = a^2/D$. Then,

$$G(t) = \frac{1}{\pi^{3/2}\bar{N}}\left[-\sqrt{\frac{t}{\tau_D}} + \exp\left(-\frac{\tau_D}{t}\right)\sqrt{\frac{t}{\tau_D}} + \sqrt{\pi}\,\mathrm{erf}\left(\sqrt{\frac{\tau_D}{t}}\right)\right]^2 \times \left[-\sqrt{\frac{t}{\omega^2\tau_D}} + \exp\left(-\frac{\omega^2\tau_D}{t}\right)\sqrt{\frac{t}{\omega^2\tau_D}} + \sqrt{\pi}\,\mathrm{erf}\left(\sqrt{\frac{\omega^2\tau_D}{t}}\right)\right] \quad (13)$$

The eq 13 expresses the theoretical model of DFSCS, and it is different from the model of DLS.[37]

Statistical Accuracy in DFSCS. In this work, we evaluated the statistical accuracy of DFSCS system from two aspects: the standard deviation (SD) and the signal-to-noise ratio (S/N). The SD is an important quantitative indicator of the statistical and systematic errors, so the accurate estimate of SD is very helpful for identifying optimal experimental conditions.[38] It is also of great importance for an accurate data evaluation especially when weighted fitting the theoretical model to the simulated or experimental data as SD determines the weight factor.[39] Here we calculate SD of DFSCS according to the algorithm proposed by Wohland et al. to compute SD of the confocal FCS.[34]

The intensity trace from one single simulation or measurement within sampling time T is divided into S subsets of an equal length T/S, and $G(t)$ is calculated for each subset. Consequently, there are S values of $G(t)$ for each delay time t, and their normalized average value is defined as

$$\bar{g}(t) = \frac{1}{S}\sum_{l=1}^{S}\frac{G_l(t) - G_{l,\infty}}{G_l(0) - G_{l,\infty}} \quad (14)$$

where $G(0)$ is the zero time value of $G(t)$, G_∞ is the convergence value of the autocorrelation function, and both of them are estimated by fitting the model to data without weighting.

Then, we compute $G(t)$ for the whole trace, and the SD is calculated by

$$\sigma(t) = \sqrt{\frac{1}{S(S-1)}\sum_{l=1}^{S}\left[\frac{G_l(t) - G_{l,\infty}}{G_l(0) - G_{l,\infty}} - \bar{g}(t)\right]^2} \quad (15)$$

Finally, the S/N for the DFSCS measurement is[40]

$$(S/N)_t = \frac{G(t)}{\sigma(t)} \quad (16)$$

For uniformity, we utilize the mean value of S/N from the first eight delay channels as the representative of that from all channels.

METHODS AND EXPERIMENTS

The Simulated System. At the beginning, we defined the conditions for computer simulations. The simulation parameters were set to be close to the counterparts employed in the real experiments described later. First, a cuboid simulation space with the size of 5.6 μm length, 5.6 μm width, and 32.2 μm height was established. Then, at the center of the simulation space we defined a virtual detection volume which was 0.8 μm length, 0.8 μm width, consistent with the size of the pixel of EMCCD, and 4.6 μm height. As the simulation space was 343 times larger than the detection volume, the influence of the boundary conditions on the calculations could be neglected.[41] If not otherwise stated, 608 particles were uniformly distributed in the simulation space as the initial state. The corresponding concentration was about 1 nM. The particle concentration was so low that each particle was considered to perform a random walk independently. The time step of the simulation was set to $\Delta t = 0.5$ ms, equal to the sampling time of the EMCCD camera used in this work.

To simulate the diffusion of particles, a displacement was added to each particle based on its current coordinates at each step. The direction of the movement was completely random, and the displacement was determined by a random variable subjects to Gaussian distribution with the center value zero and an SD = $(6D\Delta t)^{1/2}$, where D is the set diffusion coefficient. Reflecting boundary conditions were utilized.[41] When a particle left the simulation space due to diffusion, a new particle was added inside to maintain the number concentration in the simulation space constant. The new particle was located at the symmetric place of its current position, where the symmetric plane was the outside surface of the simulation space. However, the number of particles in the detection volume that was much smaller than the simulation space, still varied freely. Both the illumination intensity distribution and the collection efficiency were assumed to be homogeneous as discussed above. The intensity from a single nanoparticle collected by the detector was the product of illumination intensity, collection efficiency, scattering efficiency, and detection efficiency of the experimental system. After each step, the intensity from all nanoparticles inside the detection volume was added. The procedure was repeated at least 500 000 times, resulting in an intensity trace longer than 250 s. Further autocorrelation analysis of the intensity trace yielded the $G(t)$ curves. The simulation programs were written in Matlab (MathWorks, Inc.) and executed on a personal computer.

Apparatus. The experimental setup is based on an inverted fluorescent microscope (Olympus IX 71, Olympus Optical Co., Japan) equipped with a dark-field condenser as schematically displayed in Figure 1.[42] The illumination is provided by a halogen lamp, which is the standard light source of the bright-field microscope. The dark-field condenser forms a hollow cone of light focused on the plane of the sample. Only the light that is scattered out of this cone reaches the

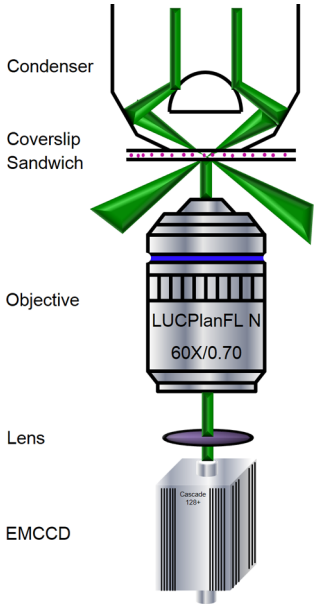

Figure 1. Schematic diagram of DFSCS setup.

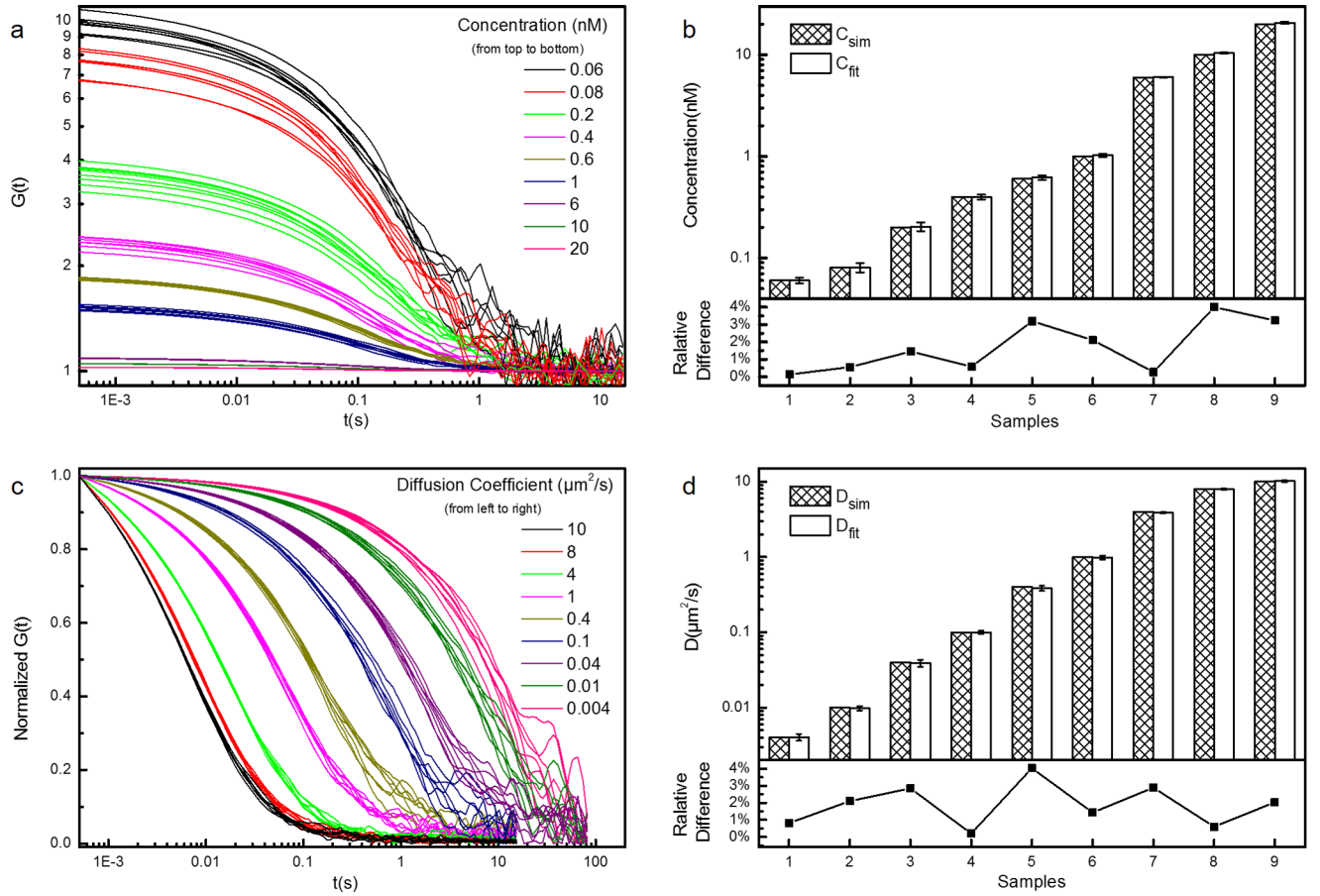

Figure 2. Simulated results. Autocorrelation curves, $G(t)$, calculated from nanoparticle samples of various simulated concentrations, C_{sim}, (a) and diffusion coefficients, D_{sim}, (c). Compare between C_{sim} with the corresponding fitted concentration, C_{fit}, (b) and between D_{sim} with the corresponding fitted diffusion coefficient, D_{fit}, (d).

objective (LUCPlanFL N 60×/0.70, Olympus Optical Co., Japan). Thus, particles on the substrate appear as bright, diffraction-limited spots on a dark background. An EMCCD camera (Cascade 128+, Roper Scientific, Inc.) is used to detect the scattered light. The camera is manipulated by the Micromanager software (http://micro-manager.org/).[43]

The imaging area of the EMCCD is 3.072 × 3.072 mm^2, and it is divided into 128 × 128 pixels yielding 24 × 24 μm^2/pixel. The state-of-the-art camera can collect more than 500 full frames of true 16-bit data per second, and faster frame rates are achievable via subregion readout or pixel binning.[13b] What's more, with the help of the solid-state disk, we can further improve the frame rate and save the data storage time. In the present work, a region of interest (ROI) of 16 × 16 pixels with 2 × 2 hardware binning is usually selected.[13b] A stack of 500 000 frames of the ROI is collected with the acquisition rate of 0.5 ms per frame for each measurement and read out as the true 16-bit data with a 12 MHz digitizer. It took <3 min to save the data in the solid-state disk to form an intensity trace for further autocorrelation analysis.

Preparation of Samples. Colloidal suspensions of citrate-coated GNPs were synthesized by reduction of chloroauric acid ($HAuCl_4$) with sodium citrate according to a reported procedure.[24a] In addition, commercial GNPs products (Ted Pella, Inc., Redding) with the diameters of 60 nm (measured by transmission electron microscopy, TEM) were also used. We utilized Herceptin (Genentech, Inc.) to functionalize GNPs to favor the cellular uptake. Herceptin was first conjugated to a linker molecule, 1,4,7,10,13,16,19,22,25,32,35,38,41,-44,47,50,53-hexadecaoxa-28,29-dithiahexapentacontanedioic acid di-*N*-succinimidyl ester (NHS-PEG disulfide, Sigma Ltd.), which had both a disulfide and succinimidyl functionalities for the respective chemisorption onto gold and the facile covalent coupling of antibody.[44] Then the Herceptin-PEG complex was conjugated with GNPs through a sulfur-containing group to form the GNPs-PEG-Herceptin conjugates. A detailed introduction of the samples preparation is provided in the Supporting Information.

Typically, 8 μL GNPs solution was dropped on a 24 × 40 mm coverslip, then another identical coverslip was placed onto the solution with slight press to make the solution uniformly spread in the gap between the two coverslips.[45] At length, vaseline was used to seal the gap in order to prevent the evaporation of the solvent. Samples prepared inside the coverslip sandwich could withstand several-hour measurements.

Besides, cell culture and GNPs-PEG-Herceptin uptake are described in the Supporting Information.

Data Analysis. We treated the minimum of an intensity trace as the background and subtracted it from every data point. $G(t)$ was calculated in the quasi-logarithmic time scale using self-written programs in Matlab, and the algorithm was in line with that of commercial correlators.[34]

The theoretical model was fitted to the simulated and experimental data using the instrumental weighting, where the weighting factor for each point was $\sigma^{-2}(t)$.[39] The adjusted coefficient of determination $Adj.R^2$ was employed as an index of goodness of fitting.

$$Adj.\ R^2 = 1 - \frac{RSS/df_{Error}(RSS)}{TSS/df_{Error}(TSS)} \tag{17}$$

where y_i is the simulated or experimental data when the delay time is x_i, $y(x_i)$ is the corresponding fitted value, $\bar{y}$ is the mean of y_i, RSS = $\sum_i[y(x_i) - y_i]^2$, TSS = $\sum_i(y_i - \bar{y})^2$, $df_{error}(RSS) = v - p$, $df_{error}(TSS) = v - 1$, v denotes the number of data points, and p denotes the number of free parameters in the fitting.

dx.doi.org/10.1021/ja410284j | J. Am. Chem. Soc. 2014, 136, 2775−2785

RESULTS AND DISCUSSION

The Simulations. The parameters, such as concentration and diffusion coefficient of nanoparticles, were initially set to simulate random diffusion. Then, simulations produced synthetic $G(t)$ curves for measurement scenarios with DFSCS conditions. Finally, these parameters could be figured out by fitting the theoretical model described in eq 13 to the synthetic $G(t)$ curves. It has been confirmed the simulation procedure adopted here can correctly reproduce the features of FCS measurements.[34] Consequently, if the theoretical model is a reasonable description of particles diffusion in DFSCS system, the fitted parameters will be in accordance with their initially set value. With that, the difference between the set value and the fitted value of a certain parameter can be regarded as an indicator of the reliability and adaptability of the model. Simulations were conducted for one-component systems varying the different concentrations, C_{sim}, and diffusion coefficients, D_{sim}. The fitted concentration and diffusion coefficients were denoted as C_{fit} and D_{fit}, respectively. We performed simulations seven times for each sample and the mean, and SD of C_{fit} as well as D_{fit} were computed. The coefficient of variation was calculated from SD/mean, and its value, at most 20%, was considered as the upper limit of precise. Similarly, the relative error $|D_{sim} - D_{fit}|/D_{sim}$ or $|C_{sim} - C_{fit}|/C_{sim}$ <10% was used as the index of accuracy.[35a]

First, we simulated nine virtual samples containing various numbers of nanoparticles in the detection volume with other parameters remaining consistent. The corresponding concentrations ranged from 0.06 to 20 nM. According to the theoretical model of DFSCS, the number of particles in the detection volume, N, is inversely proportional to the amplitude of the zero time value of $G(t)$, $G(0)$.[46] The simulated $G(t)$ curves in Figure 2a show that the amplitude of $G(0)$ decreases with increasing nanoparticles concentration as predicted. Additionally, seven $G(t)$ curves for each C_{sim} approach each other, and all the coefficients of variation of C_{fit} are below 10% as described by the error bar in Figure 2b. The mean value of C_{fit} agrees well with the corresponding C_{sim} as the largest relative error between C_{fit} and C_{sim} is <4%.

Next, the accuracy of reproducing D by simulations was studied. Nine samples with D_{sim} between 0.004 and 10 $\mu m^2/s$ were simulated, and other parameters were kept consistent. As $G(t)$ measures the correlation between values of the diffusion process at different times, the particles of lower mobility yield bigger amplitude of $G(t)$ at the identical delay time. This law can be explicitly illustrated by means of comparing the normalized $G(t)$ curves. As presented in Figure 2c, the normalized $G(t)$ curve decreases more and more slowly as D_{sim} is decreased, which agrees well with the prediction. Similarly, $G(t)$ curves for the identical samples are close to each other, and all the coefficients of variation lay below 9%. It can be found from Figure 2d that the relative error between D_{fit} and D_{sim} is at most 4%.

In summary, the simulated results demonstrate that both the coefficients of variation and the relative errors, not only for concentration estimates but also for diffusion coefficients estimates, are predominantly less than the upper limit of precision and accuracy, respectively. Hence we can arrive at the conclusion that the theoretical model proposed here is a reasonable model to describe the diffusion process of nanoparticles in a uniformly illuminated field. With this model, the DFSCS method can be used to study the dynamic information of nanoparticles.

Calibrations. Before quantitative measurements, calibrations of the DFSCS system should be conducted to determine the size of the detection volume. The progress of calibration is described in the Supporting Information. Since DFSCS is a camera-based method, the radial size of the volume (length = width = $2a$) depends on the pixel size of the camera.[47] Thus, only the height, h, needs to be calibrated. Identical calibrations were repeated five times, and the resulting h was 2.6 ± 0.4 μm.

Besides, a comparison between RLSCS[29a,b] and DFSCS was performed. The results measured on the same GNPs solutions using the two methods are summarized in Table 1. We find that

Table 1. Diffusion Coefficient D of 60 nm Diameter GNPs in Solutions with Different Glycerol Content Measured by RLSCS and DFSCS

	$D(\mu m^2/s)$	
NP solution/glycerol content	RLSCS	DFSCS
0	3.947 ± 0.177	2.020 ± 0.076
10%	2.611 ± 0.042	1.577 ± 0.086
20%	2.209 ± 0.052	1.184 ± 0.104
30%	2.070 ± 0.073	0.756 ± 0.046
40%	1.232 ± 0.060	0.474 ± 0.028
50%	0.808 ± 0.051	0.339 ± 0.042

the measured D by RLSCS is comparable to the counterpart obtained by DFSCS, which indicates that the DFSCS methodology is as reliable as the RLSCS method. The difference may be explained by the blocking effect of the coverslip surface on the movement of nanoparticles in dark-field configuration, which is similar to the results published earlier.[30] Since the height of the coverslip sandwich is micrometer-sized, the nanoparticles collide with the coverslip surface frequently. As a result, the diffusion of the nanoparticles is restricted and slower than the free diffusion just as the behaviors of nanoparticles in RLSCS.

Performance of DFSCS System. After calibrations, DFSCS measurements were carried out in GNPs solutions. The detection window was a ROI of 16 × 16 pixels with 2 × 2 hardware binning, including 64 detection volumes of 48 × 48 μm^2. Typical $G(t)$ curves measured on a 60 nm diameter GNPs solution and their fitting results are displayed in Figure 3 (the data collected by the pixels of the first column in the ROI is not shown, because it is dramatically different from that collected by other pixels even when the control measurements without any illumination are performed. The signals collected by pixels of the first column are almost zero no matter how strong the illumination intensity is. We preliminarily estimate that this phenomenon is caused by an inherent bug of the EMCCD camera or the Micromanager software), and the corresponding fitting residuals are plotted in Figure S1. No correlation is found in the negative control measured on pure water (data not shown). As seen in Figure 3, all $G(t)$ curves are smooth and similar to each other with the mean S/N ratio of 17.6, and they are well fitted with the theoretical model with $Adj.R^2$ of 0.997−0.999. The average measured concentration and D of GNPs are 1.09 ± 0.07 nM and 0.65 ± 0.067 $\mu m^2/s$, respectively, and the corresponding relative standard deviations (RSD) are 6.5% and 8.8%.

The small RSDs manifest the high parallelization of all detection volumes, so it will be possible to distinguish the even

dx.doi.org/10.1021/ja410284j | J. Am. Chem. Soc. 2014, 136, 2775−2785

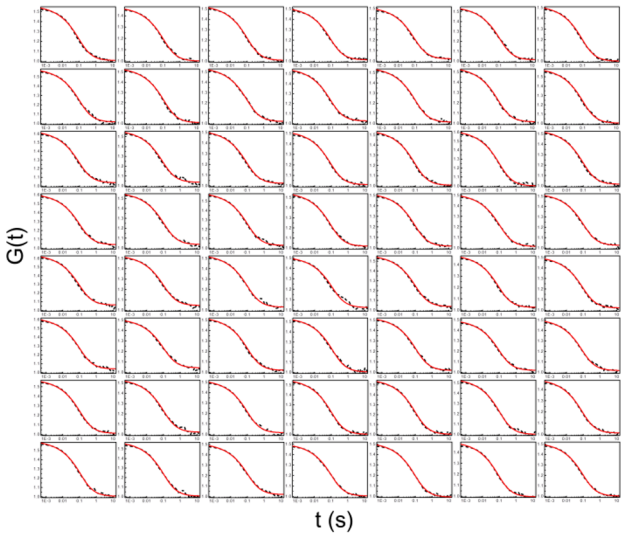

Figure 3. Autocorrelation curves measured on a 60 nm diameter GNPs sample from 56 detection volumes. Fitting curves are shown as red solid lines. The time resolution for measurements is 0.5 ms.

minor differences among various areas. This endows the DFSCS system with the ability of multiplex measurement in real time as well as spatial resolution. The RSD of D is a little larger than that of concentration on account of the nonuniformity of size, as the size owns a direct relation with D revealed by the Stokes——Einstein equation ($D = k_BT/6\pi\eta r_h$, k_B the Boltzmann constant, T the absolute temperature, η the viscosity of the solution, and r_h the hydrodynamic radius of the molecule). Another significant advantage of DFSCS endowed by EMCCD camera is that it is flexible to vary the size and the number of detection volumes by adjusting the magnification of the objective and the number of selected pixels, pixel hardware binning, and software binning.[30] Software binning exhibits special flexibility as it is carried out after measurements.

It is noted that the characteristic diffusion time (τ_d) is about 100 ms, in turn the ratio of the temporal resolution ($\Delta\tau$ = 0.5 ms) versus τ_d, $\Delta\tau/\tau_d$, is 0.005, which is much smaller than the critical value (0.1) for accurate measurements put forward by Wohland et al.[35a] In other words, the frame acquisition rate of EMCCD is adequate for the current measurements, although it is limited compared with 0.1−0.2 μs for the avalanche photo diode that is the most frequently used detector of confocal FCS.[48]

Sensitivity of DFSCS System. In order to study the sensitivity of DFSCS system, the dependence of $G(t)$ upon the concentration and D of GNPs as well as other factors were investigated both in theory and in experiments.

As the derivative measures how much one quantity is changing in response to changes in another quantity,[49] we tentatively put forward the first partial derivative of $G(t)$, dG, respect to a certain factor as the index of the sensitivity of $G(t)$ to this factor. The detail description is found in the Supporting Information. From the calculated results depicted in Figure 4 and Figure S2, we can arrive at three conclusions. First, dG of DFSCS (Figure 4a) is comparable to that of confocal FCS respect to the same factor (Figure S2, calculated with the same parameters as used for DFSCS). Specifically, as shown in Figure 4b, the amplitude of dG respect to N as well as D of DFSCS is close to the counterpart of confocal FCS. Accordingly, DFSCS

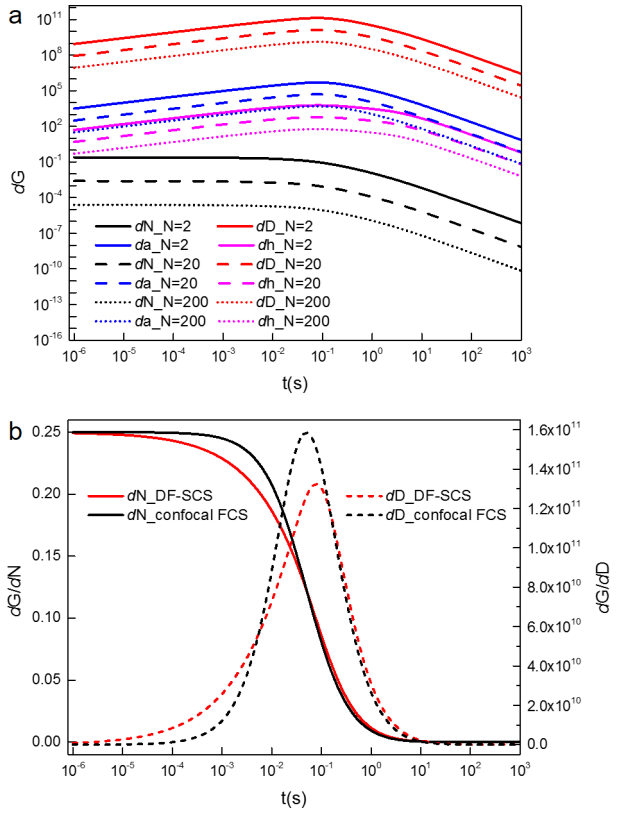

Figure 4. (a) The first partial derivatives of $G(t)$, dG, in DFSCS respect to each variable: particle number in the detection volume, N, diffusion coefficient, D, length of detection volume, a, height of detection volume, h. N is set to be 2, 20, and 200, respectively. (b) Comparison between dG respect to N as well as to D in confocal FCS and the counterparts in DFSCS. N = 2.

is as sensitive as confocal FCS in theory. Second, the amplitude of dG increases as N decreases, which means that lower concentration yields higher sensitivity. This result provides us a guideline for identification of optimal experimental conditions that high signal-to-noise ratio can be achieved by means of decreasing the particle number in the detection volume.[2] Third, the amplitude of dG respect to a (or ω_{xy}) is larger than that to h (or ω_z), implying that G is more sensitive to the radial dimension than the axial dimension of the detection volume. Our finding corroborates the reported conclusion that the accuracy of determining the value of h or ω_z is lower than that of a or ω_{xy}.[8a] To sum up, DFSCS exhibits a comparable performance of sensitivity to confocal FCS in theory.

Furthermore, experimental tests in practice were performed. Under the identical conditions, 60 nm diameter GNPs solutions of different concentrations or viscosities were measured. Measurements on a ROI of 16 × 16 pixels with 2 × 2 hardware binning with the acquisition rate of 0.5 ms per frame were carried out at least 3 times for each sample.

First, an original GNPs solution with the concentration about 3 nM was diluted continuously to vary the concentration, and other properties were left unchanged. The corresponding concentrations ranged from about 0.375 to 3.000 nM. The measured results by DFSCS are expressed in Figure 5a. Clearly, the measured concentration is proportional to the relative concentration (C_r) that is the inverse of the dilution multiple as expected. The $Adj.R^2$ of linear fitting is 0.972, indicating a good linearity. This result manifests that the DFSCS method, similar

dx.doi.org/10.1021/ja410284j | J. Am. Chem. Soc. 2014, 136, 2775−2785

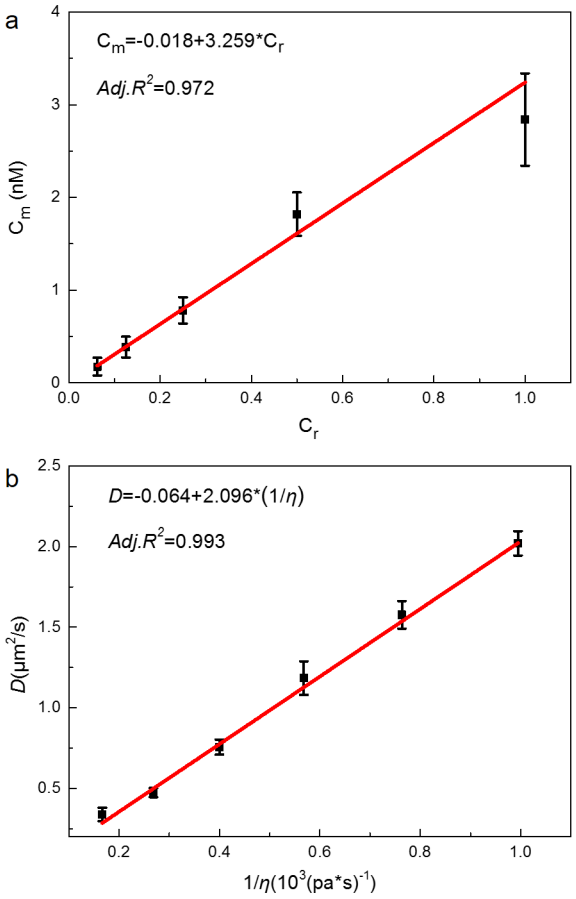

Figure 5. (a) Measured concentrations of GNPs solutions which were diluted by various factors. C_r denotes the relative concentration that is the inverse of the dilution multiple, and C_m is the measured concentration. (b) Typical plots of diffusion coefficient, D, versus the inverse of the viscosity, η, of the GNPs solution.

to traditional confocal FCS, is of reliable sensitivity to the concentration changes even smaller than 1 nM.

Next, we tested the responses of DFSCS system to diffusion processes with different diffusion rates. From the Stokes–Einstein equation, it is known that D of particles is inversely proportional to η of the solution. Thus we studied the relationships between D and η by single factor analysis. Six GNPs solutions with different concentrations of glycerol were measured. The measured D located between 0.338 and 2.020 $\mu m^2/s$. As demonstrated in Figure 5b, the D increases linearly with the inverse of η as expected, with the corresponding $Adj.R^2$ of 0.993. The relationship between D with η revealed by the experimental results agrees well with the Stokes–Einstein equation, suggesting that DFSCS is a powerful tool to research the dynamic processes of nanoparticles.

Until now, DFSCS has exhibited its capacity to study the diffusion behavior of nanoparticles *in vitro* as a compartmentalized quantification and dynamics monitoring method. Next, the suitability of DFSCS system for biological applications is investigated by measuring the dynamic information of intracellular GNPs.

Measurements on the Dynamic Behaviors of GNPs in Live Cells. The cervical cancer SiHa cell line was utilized as the model. Herceptin acted as delivery agent of 18 nm diameter GNPs through the linker molecule NHS-PEG disulfide. The ζ potential of GNPs was −52.70 ± 0.78 mV, and it significantly increased to −15.3 ± 2.13 mV after reaction with the PEG-Herceptin complex, indicating the formation of GNPs-PEG-Herceptin conjugates. Joseph et al. found that GNPs were mainly internalized into the endosome and lysosome with the help of Herceptin.[24b] TEM images (Figure 6a,b) clearly display

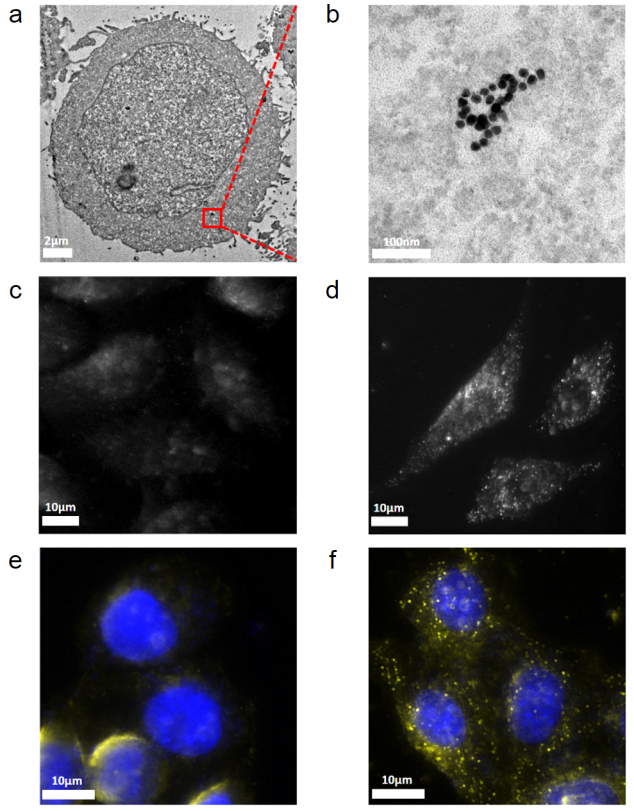

Figure 6. Cell imaging. TEM image of cells treated with GNPs-PEG-Herceptin conjugates (a) and boxed regions are enlarged in adjacent panels (b). Dark-field images of untreated control cells (c) and cells treated with GNPs-PEG-Herceptin conjugates (d). Combination of dark-field image color-coded as yellow and fluorescence image color-coded as blue of untreated control cells (e) and the cells treated with GNPs-PEG-Herceptin conjugates (f). Cells were stained with DAPI, which was a dye emitting strong bluish white fluorescence.

the existence of intracellular GNPs and that the particles inside the organelle are in a nonaggregated state. This result is consistent with the conclusion that GNPs functionalized by Herceptin are stable even when residing in acidic environments such as the endosome and lysosome.[50] It can be seen in Figure 6d,f (cell nucleus were stained with DAPI, 4′, 6-diamidino-2-phenylindole) that intracellular GNPs emit strong scattered light in the dark-field microscope, so we can clearly observe their distribution. It must be mentioned that the cells themselves, especially organelles, also emit scattered light, but their intensity is much lower than that of GNPs (Figure 6c,e). What's more, the scattered light of GNPs exhibits a characteristic color depending on the particles size and sharp.[51] As a result, using the excitation light source of the reasonable power, the intracellular GNPs can be easily distinguished from the negligible background, and the intracellular GNPs-located regions can be measured selectively.

Representative $G(t)$ curves measured from both the intracellular regions with GNPs and without GNPs are presented in Figure 7a. No correlation is found in the negative

dx.doi.org/10.1021/ja410284j | J. Am. Chem. Soc. 2014, 136, 2775–2785

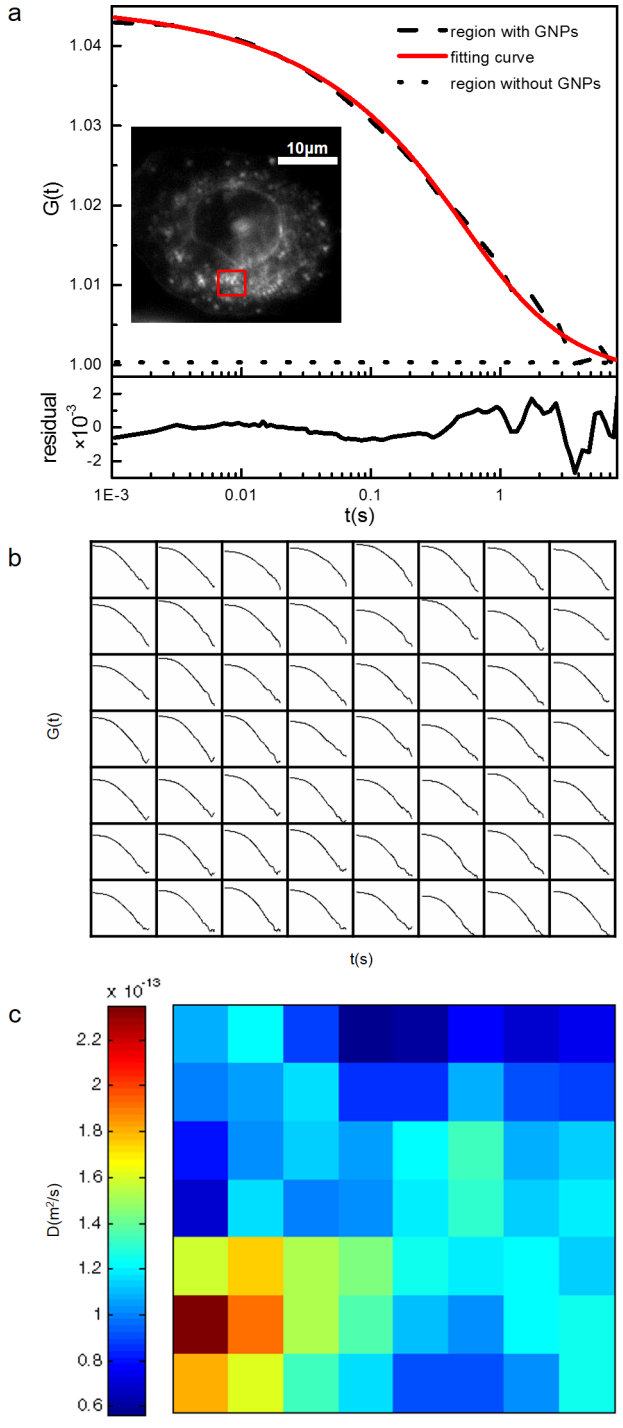

Figure 7. Decay of autocorrelation curves, $G(t)$, measured on an intracellular region with GNPs (dashed line) and its fitting curve (continuous line) to eq 13 as well as measured on a region without GNPs (dotted line) (a). The fitting residuals are shown in the lower panels. Maps of $G(t)$ (b) and the diffusion coefficient, D, (c) obtained from the small region labeled by a red rectangle (inserted in (a)).

control measured on the region without GNPs, however, the $G(t)$ curves measured on GNPs located regions exhibit the typical profile of the autocorrelation curves. We studied the compartmentalized dynamics of intracellular GNPs. $G(t)$ curves from all 56 detection volumes are shown in Figure 7b, and they are well fitted with the theoretical mode with $Adj.R^2$ of 0.996–0.999. The value of the obtained D ranges between 0.056 and 0.235 $\mu m^2/s$. From the D map (Figure 7c), it is clearly that D values are of great variety. The various D indicates that the diffusion rates of GNPs in different intracellular areas are not uniform, in sharp contrast to the high parallelization of the measured results on GNPs solution as mentioned above. Therefore, we may conclude that the intracellular environment is complex and heterogeneous.

Up to now, multiplex measurements of intracellular dynamic information with imaging enabled by DFSCS have been achieved, and the spatially resolved ability of the new method has contributed to distinguish different microenvironments. In the next section, further study on the heterogeneous intracellular environment by diffusion law will be carried on.

Characterizing the Heterogeneity of Intracellular Environment by Diffusion Laws. The FCS diffusion law, which describes the dependence of the transition time τ_D of a particle through an observation area on the size of the area A, is an excellent tool to study the heterogeneity of a complex system.[35b,52] Note that A is the actual area over which particles are measured, and it is defined as the convolution of the detection area with the point spread function of the optical system. For free diffusion, one can expect to obtain a linear function between τ_D and A: the curve $\tau_D = f(A)$ will intercept the time origin. Any nonzero intercept is an indication of the hindered diffusion within heterogeneous environment, and the sign of the intercept depends on the diffusion mode. Specifically, dynamic partition into micro domains results in a positive intercept, and a negative value corresponds to hindered diffusion due to barriers of the cytoskeleton meshwork. The FCS diffusion law has been already successfully corroborated and widely applied to study the architecture of the live cell.[53]

Here we extend the application of the FCS diffusion law to the DFSCS method. Since the distribution of the illumination intensity in the dark-field microscope is homogeneous, A is equal to the detection area and in turn the size of the pixel employed as the detection volume. As a camera-based method, DFSCS has the advantage that the entire diffusion law plots over various detection areas could be achieved by changing the magnification of objective, pixel hardware binning, and software binning postacquisition. We made use of GNPs as the probe to study the heterogeneity of both GNPs solutions and intracellular environment. The diffusion laws were calculated based on the same data by varying the detection area using software binning (1×1–5×5). For each binning, all possible areas in a measurement were used for the evaluation. The diffusion law is visualized by plotting A/D versus A, as the parameter A/D is proportional to the transition time τ_D. Typical results are depicted in Figure 8. For GNPs solutions, A/D increases linearly with A, and the intercepts upon extrapolation are nearly zero, which is an indication of the homogeneity of the GNPs solution. In contrast, for the SiHa cell a strict positive intercept is obtained, indicating that there exist micro domains which hinder the diffusion of GNPs. So the complex of intracellular environment is verified again, which echoes the heterogeneity of D maps shown in Figure 7d. The preliminary results demonstrate that DFSCS is a powerful method to investigate the heterogeneous system with the help of the diffusion law.

■ CONCLUSIONS

In this work, we described a new tempo-spatially resolved fluctuation spectroscopy using the dark-field microscope and an EMCCD camera as the detector. The reliability and adaptability of the theoretical model of DFSCS proposed here have been

dx.doi.org/10.1021/ja410284j | J. Am. Chem. Soc. 2014, 136, 2775–2785

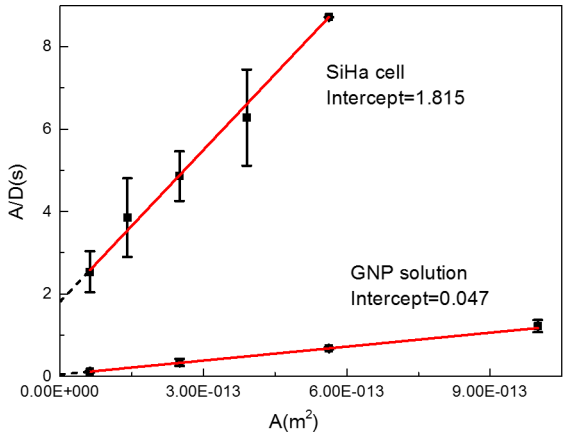

Figure 8. Experimental FCS diffusion laws obtained for GNPs in solution and inside SiHa cells. Red lines are the respective linear fittings of A/D versus A, where A is the size of the area, and D is the diffusion coefficient. Black dash lines are the extrapolations of fitting curves to zero detection area to make the time intercept more visible.

verified by both the simulated and experimental results. DFSCS has three important features: First, compared with the complex and expensive confocal configuration of the traditional FCS, the setup of DFSCS is much easier and more economically achievable by introducing a dark-field condenser to the frequently used bright-field microscope. Second, DFSCS is free from fluorescence bleaching, blinking, and saturation as the scattered light but not the fluorescence is employed as the probe, making it possible to research long-term dynamic processes. Third, an EMCCD is utilized as an array detector, and each pixel of the camera is turned into an individual detection channel, endowing DFSCS with the ability to study the heterogeneous system as a multiplex, high-throughput, and spatially resolved technique. The investigation on the intracellular GNPs and the heterogeneity of the intracellular environment reveals the potential of DFSCS for biological applications. Our preliminary results have documented that DFSCS is a simple, economical, free from fluorescence bleaching, multiplex, high-throughput, and spatially resolved method to study the dynamic behaviors of nonfluorescent nanoparticles *in vitro* and *in vivo*. To the best of our knowledge, this is also the first time that the white light is used as the light source of fluctuation correlation spectroscopy. It should be noted that the current DFSCS system has a limited temporal resolution constrained by the frame acquisition rate of EMCCD. Future advances in EMCCD camera technology or the replacement by the complementary metal oxide semiconductor camera (CMOS) may dramatically improve the temporal resolution of DFSCS.

■ ASSOCIATED CONTENT

Ⓢ Supporting Information

Description of the material included. This material is available free of charge via the Internet at http://pubs.acs.org.

■ AUTHOR INFORMATION

Corresponding Author

jicunren@sjtu.edu.cn

Notes

The authors declare no competing financial interest.

■ ACKNOWLEDGMENTS

This work was financially supported by NSFC (grants 21075081, 20905048, 21135004, and 21327004) and the National Basic Research Program of China (grant 2009CB930400).

■ REFERENCES

(1) (a) Webber, C.; Zbilut, J. P. *J. Appl. Physiol.* **1994**, *76*, 965. (b) Goldberger, A. L.; Amaral, L. A.; Hausdorff, J. M.; Ivanov, P. C.; Peng, C.-K.; Stanley, H. E. *Proc. Natl. Acad. Sci. U.S.A.* **2002**, *99*, 2466.
(2) Eigen, M.; Rigler, R. *Proc. Natl. Acad. Sci. U.S.A.* **1994**, *91*, 5740.
(3) (a) Magde, D.; Elson, E.; Webb, W. W. *Phys. Rev. Lett.* **1972**, *29*, 705. (b) Elson, E. L.; Magde, D. *Biopolymers* **1974**, *13*, 1. (c) Magde, D.; Elson, E. L.; Webb, W. W. *Biopolymers* **1974**, *13*, 29.
(4) (a) Sasmal, D. K.; Mandal, A. K.; Mondal, T.; Bhattacharyya, K. *J. Phys. Chem. B* **2011**, *115*, 7781. (b) Petrášek, Z.; Schwille, P. *Biophys. J.* **2008**, *94*, 1437. (c) Gell, C.; Brockwell, D. J.; Beddard, G. S.; Radford, S. E.; Kalverda, A. P.; Smith, D. A. *Single Mol.* **2001**, *2*, 177. (d) Korlach, J.; Schwille, P.; Webb, W. W.; Feigenson, G. W. *Proc. Natl. Acad. Sci. U.S.A.* **1999**, *96*, 8461.
(5) (a) Kettling, U.; Koltermann, A.; Schwille, P.; Eigen, M. *Proc. Natl. Acad. Sci. U.S.A.* **1998**, *95*, 1416. (b) Wohland, T.; Friedrich, K.; Hovius, R.; Vogel, H. *Biochemistry* **1999**, *38*, 8671. (c) Yao, J.; Munson, K. M.; Webb, W. W.; Lis, J. T. *Nature* **2006**, *442*, 1050. (d) García-Sáez, A. J.; Schwille, P. *Methods* **2008**, *46*, 116.
(6) (a) Malvezzi-Campeggi, F.; Jahnz, M.; Heinze, K. G.; Dittrich, P.; Schwille, P. *Biophys. J.* **2001**, *81*, 1776. (b) Huang, S.; Heikal, A. A.; Webb, W. W. *Biophys. J.* **2002**, *82*, 2811. (c) Schwille, P.; Kummer, S.; Heikal, A. A.; Moerner, W.; Webb, W. W. *Proc. Natl. Acad. Sci. U.S.A.* **2000**, *97*, 151. (d) Widengren, J.; Seidel, C. A. M. *Phys. Chem. Chem. Phys.* **2000**, *2*, 3435. (e) Heikal, A. A.; Hess, S. T.; Webb, W. W. *Chem. Phys.* **2001**, *274*, 37. (f) Heikal, A. A.; Hess, S. T.; Baird, G. S.; Tsien, R. Y.; Webb, W. W. *Proc. Natl. Acad. Sci. U.S.A.* **2000**, *97*, 11996. (g) Haupts, U.; Maiti, S.; Schwille, P.; Webb, W. W. *Proc. Natl. Acad. Sci. U.S.A.* **1998**, *95*, 13573. (h) Widengren, J.; Mets, Ü.; Rigler, R. *Chem. Phys.* **1999**, *250*, 171.
(7) (a) Latypov, R. F.; Cheng, H.; Roder, N. A.; Zhang, J.; Roder, H. *J. Mol. Biol.* **2006**, *357*, 1009. (b) Lenne, P. F.; Wawrezinieck, L.; Conchonaud, F.; Wurtz, O.; Boned, A.; Guo, X. J.; Rigneault, H.; He, H. T.; Marguet, D. *EMBO J.* **2006**, *25*, 3245. (c) Sherman, E.; Haran, G. *Proc. Natl. Acad. Sci. U.S.A.* **2006**, *103*, 11539. (d) Neuweiler, H.; Johnson, C. M.; Fersht, A. R. *Proc. Natl. Acad. Sci. U.S.A.* **2009**, *106*, 18569.
(8) (a) Rigler, R.; Mets, Ü.; Widengren, J.; Kask, P. *Eur. Biophys. J.* **1993**, *22*, 169. (b) Weiss, S. *Science* **1999**, *283*, 1676. (c) Medina, M. Á.; Schwille, P. *Bioessays* **2002**, *24*, 758.
(9) (a) Kim, S. A.; Heinze, K. G.; Schwille, P. *Nat. Methods* **2007**, *4*, 963. (b) Ries, J.; Petrov, E. P.; Schwille, P. *Biophys. J.* **2008**, *95*, 390. (c) Elson, E. L. *Methods Enzymol.* **2013**, *518*, 11.
(10) Enderlein, J.; Gregor, I.; Patra, D.; Dertinger, T.; Kaupp, U. B. *ChemPhysChem* **2005**, *6*, 2324.
(11) (a) Weisshart, K.; Jungel, V.; Briddon, S. J. *Curr. Pharm. Biotechnol.* **2004**, *5*, 135. (b) Domingos, R. F.; Baalousha, M. A.; Ju-Nam, Y.; Reid, M. M.; Tufenkji, N.; Lead, J. R.; Leppard, G. G.; Wilkinson, K. J. *Environ. Sci. Technol.* **2009**, *43*, 7277. (c) Connolly, C. *Sens. Rev.* **2005**, *25*, 252.
(12) Elson, E. *Methods Enzymol.* **2013**, *518*, 1.
(13) (a) Thompson, N. L.; Burghardt, T. P.; Axelrod, D. *Biophys. J.* **1981**, *33*, 435. (b) Kannan, B.; Guo, L.; Sudhaharan, T.; Ahmed, S.; Maruyama, I.; Wohland, T. *Anal. Chem.* **2007**, *79*, 4463.
(14) Digman, M. A.; Brown, C. M.; Sengupta, P.; Wiseman, P. W.; Horwitz, A. R.; Gratton, E. *Biophys. J.* **2005**, *89*, 1317.
(15) Eggeling, C.; Ringemann, C.; Medda, R.; Schwarzmann, G.; Sandhoff, K.; Polyakova, S.; Belov, V. N.; Hein, B.; von Middendorff, C.; Schonle, A.; Hell, S. W. *Nature* **2009**, *457*, 1159.
(16) Wohland, T.; Shi, X.; Sankaran, J.; Stelzer, E. H. *Opt. Express* **2010**, *18*, 10627.

(17) Zsigmondy, R.; Alexander, J. *Colloids and the ultramicroscope: a manual of colloid chemistry and ultramicroscopy*; J. Wiley & Sons: New York, 1909.
(18) van Dijk, M. A.; Lippitz, M.; Orrit, M. *Acc. Chem. Res.* **2005**, *38*, 594.
(19) Drummen, G. P. *Molecules* **2012**, *17*, 14067.
(20) (a) Widengren, J.; Chmyrov, A.; Eggeling, C.; Löfdahl, P.-Å.; Seidel, C. A. M. *J. Phys. Chem. A* **2006**, *111*, 429. (b) Eggeling, C.; Widengren, J.; Rigler, R.; Seidel, C. A. M. *Anal. Chem.* **1998**, *70*, 2651.
(21) (a) Michalet, X.; Pinaud, F. F.; Bentolila, L. A.; Tsay, J. M.; Doose, S.; Li, J. J.; Sundaresan, G.; Wu, A. M.; Gambhir, S. S.; Weiss, S. *Science* **2005**, *307*, 538. (b) Jamieson, T.; Bakhshi, R.; Petrova, D.; Pocock, R.; Imani, M.; Seifalian, A. M. *Biomaterials* **2007**, *28*, 4717.
(22) (a) Kirchner, C.; Liedl, T.; Kudera, S.; Pellegrino, T.; Muñoz Javier, A.; Gaub, H. E.; Stölzle, S.; Fertig, N.; Parak, W. J. *Nano Lett.* **2004**, *5*, 331. (b) Derfus, A. M.; Chan, W. C. W.; Bhatia, S. N. *Nano Lett.* **2004**, *4*, 11.
(23) (a) Jans, H.; Huo, Q. *Chem. Soc. Rev.* **2012**, *41*, 2849. (b) Murphy, C. J.; Gole, A. M.; Stone, J. W.; Sisco, P. N.; Alkilany, A. M.; Goldsmith, E. C.; Baxter, S. C. *Acc. Chem. Res.* **2008**, *41*, 1721. (c) Lee, K.-S.; El-Sayed, M. A. *J. Phys. Chem. B* **2006**, *110*, 19220. (d) Zhang, L.; Li, Y.; Li, D. W.; Jing, C.; Chen, X.; Lv, M.; Huang, Q.; Long, Y. T.; Willner, I. *Angew. Chem., Int. Ed.* **2011**, *50*, 6789. (e) Panchapakesan, B.; Book-Newell, B.; Sethu, P.; Rao, M.; Irudayaraj, J. *Nanomedicine* **2011**, *6*, 1787.
(24) (a) He, H.; Xie, C.; Ren, J. *Anal. Chem.* **2008**, *80*, 5951. (b) Chen, J.; Irudayaraj, J. *ACS Nano* **2009**, *3*, 4071. (c) Wang, Y.; Chen, J.; Irudayaraj, J. *ACS Nano* **2011**, *5*, 9718.
(25) Li, Y.; Jing, C.; Zhang, L.; Long, Y.-T. *Chem. Soc. Rev.* **2012**.
(26) (a) Schultz, S.; Smith, D. R.; Mock, J. J.; Schultz, D. A. *Proc. Natl. Acad. Sci. U.S.A.* **2000**, *97*, 996. (b) Michaels, A. M.; Nirmal, M.; Brus, L. E. *J. Am. Chem. Soc.* **1999**, *121*, 9932.
(27) Kreibig, U.; Vollmer, M. *Optical properties of metal clusters*; Springer: Berlin, 1995.
(28) (a) Hulst, H. C.; van de Hulst, H. C. *Light scattering: by small particles*; Wiley: NewYork, 1957. (b) Bohren, C. F.; Huffman, D. R. *Absorption and Scattering of Light by Small Particles*; Wiley-Interscience: NewYork, 1983.
(29) (a) Wang, K.; Qiu, X.; Dong, C.; Ren, J. *ChemBioChem* **2007**, *8*, 1126. (b) Lan, T.; Dong, C.; Huang, X.; Ren, J. *Analyst* **2011**, *136*, 4247. (c) Lan, T.; Dong, C.; Huang, X.; Ren, J. *Talanta* **2013**, *116*, 501.
(30) Liu, H.; Dong, C.; Huang, X.; Ren, J. *Anal. Chem.* **2012**, *84*, 3561.
(31) (a) Schultz, S.; Smith, D. R.; Mock, J. J.; Schultz, D. A. *Proc. Natl. Acad. Sci. U.S.A.* **2000**, *97*, 996. (b) Xiao, L.; Wei, L.; He, Y.; Yeung, E. S. *Anal. Chem.* **2010**, *82*, 6308. (c) Xiao, L.; Wei, L.; Cheng, X.; He, Y.; Yeung, E. S. *Anal. Chem.* **2011**, *83*, 7340. (d) Xiao, L.; Qiao, Y.; He, Y.; Yeung, E. S. *J. Am. Chem. Soc.* **2011**, *133*, 10638.
(32) Oleg, K.; Grégoire, B. *Rep. Prog. Phys.* **2002**, *65*, 251.
(33) Haustein, E.; Schwille, P. *Annu. Rev. Bioph. Biom.* **2007**, *36*, 151.
(34) Wohland, T.; Rigler, R.; Vogel, H. *Biophys. J.* **2001**, *80*, 2987.
(35) (a) Sankaran, J.; Bag, N.; Kraut, R. S.; Wohland, T. *Anal. Chem.* **2013**, *85*, 3948. (b) Bag, N.; Sankaran, J.; Paul, A.; Kraut, R. S.; Wohland, T. *ChemPhysChem* **2012**, *13*, 2784.
(36) Capoulade, J.; Wachsmuth, M.; Hufnagel, L.; Knop, M. *Nat. Biotechnol.* **2011**, *29*, 835.
(37) Goldburg, W. *Am. J. Phys.* **1999**, *67*, 1152.
(38) (a) Koppel, D. E. *Phys. Rev. A* **1974**, *10*, 1938. (b) Kask, P.; Günther, R.; Axhausen, P. *Eur. Biophys. J.* **1997**, *25*, 163.
(39) Dean, P. N.; Jett, J. H. *J. Cell. Sci.* **1974**, *60*, 523.
(40) Starchev, K.; Ricka, J.; Buffle, J. *J. Colloid Interface Sci.* **2001**, *233*, 50.
(41) Starchev, K.; Zhang, J.; Buffle, J. *J. Colloid Interface Sci.* **1998**, *203*, 189.
(42) He, H.; Ren, J. *Talanta* **2008**, *77*, 166.
(43) Stuurman, N.; Amdodaj, N.; Vale, R. *Microsc. Today* **2007**, *15*, 42.
(44) Huang, X.; Ren, J. *Anal. Chim. Acta* **2011**, *686*, 115.
(45) Wennmalm, S.; Widengren, J. *J. Am. Chem. Soc.* **2012**, *134*, 19516.
(46) Webb, W. W.; Hess, S. T.; Huang, S. H.; Heikal, A. A. *Biochemistry* **2002**, *41*, 697.
(47) Ries, J.; Schwille, P. *Bioessays* **2012**, *34*, 361.
(48) Kannan, B.; Har, J. Y.; Liu, P.; Maruyama, I.; Ding, J. L.; Wohland, T. *Anal. Chem.* **2006**, *78*, 3444.
(49) Rosenbaum, R. A.; Johnson, G. P. *Calculus: basic concepts and applications*; Cambridge University Press: NewYork, 1984.
(50) Lee, R. J.; Wang, S.; Low, P. S. *Biochim. Biophys. Acta* **1996**, *1312*, 237.
(51) Orendorff, C. J.; Sau, T. K.; Murphy, C. J. *Small* **2006**, *2*, 636.
(52) Wawrezinieck, L.; Rigneault, H.; Marguet, D.; Lenne, P.-F. *Biophys. J.* **2005**, *89*, 4029.
(53) Lenne, P.-F.; Wawrezinieck, L.; Conchonaud, F.; Wurtz, O.; Boned, A.; Guo, X.-J.; Rigneault, H.; He, H.-T.; Marguet, D. *EMBO J.* **2006**, *25*, 3245.